

Atomically Resolved Observation of Continuous Interfaces between As-grown MoS₂ Monolayer and WS₂/MoS₂ Heterobilayer on SiO₂

Fan Zhang^{1†}, Zhixing Lu^{2†}, Yichul Choi¹, Haining Liu³, Husong Zheng¹, Liming Xie³,
Kyungwha Park¹, Liying Jiao^{2*}, Chenggang Tao^{1*}

¹Department of Physics, Virginia Tech, Blacksburg, Virginia 24061, USA

²Department of Chemistry, Tsinghua University, Beijing 100084, China

³Key Laboratory of Standardization and Measurement for Nanotechnology of Chinese Academy of Sciences, National Center for Nanoscience and Technology, Beijing 100190, China

[†]These authors contributed equally to this work.

*Corresponding to: lyjiao@mail.tsinghua.edu and cgtao@vt.edu.

Abstract

Van der Waals (vdW) heterostructures synthesized through the chemical vapor deposition (CVD) method allow creation and tuning of intriguing electronic and optical properties of two-dimensional (2D) materials. Especially, local structures in the heterostructures, such as interfaces, edges and point defects, are critical for their wide range of potential application. However, up to now atomic scale measurements of local structures in as-grown 2D heterostructures on insulating substrates are still rare. Here we report our scanning tunneling microscopy (STM) and spectroscopy (STS) study of as-grown MoS₂ monolayer and WS₂/MoS₂ heterobilayer on SiO₂. The heterobilayer appears smoother than the MoS₂ monolayer, with root mean square (RMS) roughness of 0.230 nm in the former and 0.329 nm in the latter. For the first time to our knowledge, we directly observed a novel type of continuous interfaces between the MoS₂ monolayer and the top layer of the heterobilayer with atomic resolution. Our STS results and density functional theory (DFT) calculations revealed the band gaps of the heterobilayer and the

MoS₂ monolayer. The finding of the continuous interfaces and the systematic characterizations could have significant impacts on optimizing and designing new 2D heterostructures.

Keywords: 2D heterostructures, transition metal dichalcogenides, interface, roughness, scanning tunneling microscopy, and scanning tunneling spectroscopy.

Introduction

Two-dimensional (2D) transition metal dichalcogenides (TMDs), ranging from metals to semiconductors, have attracted a huge amount of research efforts due to their unique properties e.g., charge density waves, direct band gaps, and valleytronics¹⁻³. These properties are critical for building electronic, spintronic and optical devices, such as single photoemission devices, monolayer TMD transistors and photodetectors⁴⁻¹¹. Beyond structures composed of single chemical component, heterostructures made of distinct layers bound by van der Waals (vdW) interlayer interaction define a new category of 2D materials, which often host novel physical properties not found in the constituent parts. In practice, designed vdW heterostructures with desirable properties will broadly extend novel applications of 2D materials and constitute central building blocks of future electronic and optoelectronic devices¹². In the past years, vdW heterostructures, such as MoS₂/graphene and WS₂/MoS₂, have been intensively studied¹²⁻¹⁴. Among the synthesized vdW heterostructures, WS₂/MoS₂ heterobilayer (Fig. 1a), particularly demonstrates interesting optical and electronic behaviors such as ultrafast interlayer photon transfer¹⁴, and can be used as heterojunction transistors and solar cells¹⁵⁻¹⁷.

VdW heterostructures can be composed through mechanical stacking of individual single-component layers^{12, 18}. However, mechanical stacking suffers from limited sizes and randomly generated locations of individual exfoliated flakes. Such a preparation procedure is hence neither scalable nor controllable, and is impractical for applications. This problem finds a solution in the chemical vapor deposition (CVD), a recently developed method for synthesizing vdW heterostructures¹⁹⁻²¹. For WS₂/MoS₂ heterostructures, both vertical and lateral configurations have been synthesized through CVD^{14, 20-23}. In the vertical WS₂/MoS₂ heterostructures, it was believed that the WS₂ layer lies on top of the MoS₂ layer with open edges²⁰. However, direct evidence for such interfacial structures at the atomic scale has yet been missing, mainly due to

technical challenges. For example, transmission electron microscopy⁶, another major probing technology with atomic resolution, cannot image as-grown samples directly without transferring. However, the transferring process usually alters certain properties of the as-grown samples, such as roughness and strain induced by the growth substrate.

In this work, we used scanning tunneling microscopy/spectroscopy (STM/STS) combined with an optical localization method to investigate the interfaces between the as-grown MoS₂ monolayer and WS₂/MoS₂ heterobilayer on SiO₂ prepared via CVD. Roughness of the heterobilayer was determined to be 0.230 ± 0.021 nm, compared with a roughness of 0.329 ± 0.033 nm in the MoS₂ monolayer. At the interface between the MoS₂ monolayer and the heterobilayer, we observed continuation of the top layer of the heterobilayer into the MoS₂ monolayer. To our best knowledge, it was the first atomically resolved observation of such a closed, rather than open, interface between the monolayer and the top layer of the heterobilayer, indicating that the two layers probably connected via covalent bonds. This observation contradicts the previous description of the interface, i.e., the top layer (e.g., WS₂) staying on the bottom layer (e.g., MoS₂) with an open edge. This finding is important for understanding the growth mechanism of 2D heteromaterials and could potentially explain some transport and optical properties of these materials. We further characterized the electronic properties of the MoS₂ monolayer, the heterobilayer, as well as the continuous interface between them. Our results could be crucial for device-related applications involving CVD-synthesized 2D materials and vdW heterostructures.

Results and discussions

The WS₂/MoS₂ heterobilayer was synthesized via CVD²⁴. The optical and atomic force microscopy (AFM) images showed typical WS₂/MoS₂ heterobilayer islands surrounded by MoS₂ monolayers (Fig. 1b). The heterobilayer islands primarily have triangular shape, indicating a S-rich condition in the growth processes²⁵. The WS₂/MoS₂ heterobilayer typically was assumed with a twisted angle of 0° or 60°, corresponding to AA' and AB stacking, respectively. To confirm the components of the monolayer and bilayer regions, we performed Raman (Figs. 1c-e) and photoluminescence² measurements (Fig S3). In the Raman spectrum (Fig. 1c), the high-frequency peaks are derived from the MoS₂ and WS₂ layers in the heterobilayer. The four low-

frequency peaks corresponded to the shear modes (17.25 cm^{-1} and 22.97 cm^{-1}) and the breathing modes (28.68 cm^{-1} and 37.66 cm^{-1}) caused by the interlayer interactions within the heterobilayer, as illustrated in Fig. 1d. The Raman and PL mapping (Figs. 1e, S3) images clearly distinguished regions of MoS₂ monolayer from those of WS₂/MoS₂ heterobilayer. Since the heterobilayer was formed by the sequential growth of MoS₂ and WS₂¹⁵, the WS₂ layer is expected to be on the top of the MoS₂ layer. To confirm the stacking order of these two layers, we etched the heterobilayers with oxygen at a temperature of 320 °C and identified the compositions of the two layers based on their distinctive oxidation behaviors (Fig. 1f). Although both MoS₂ and WS₂ can be oxidized at this temperature, the oxidation products of MoO_x were vaporized while the WO_x remained on the samples as a result of their dramatically different sublimation temperature¹⁵. Since triangular etching pits were only observed in the single layer region (Fig. 1f), we can conclude that the bottom layer is MoS₂. In addition, after etching, the Raman intensity for MoS₂ dramatically decreased in the single layer region, while it remained the same in the bilayer region (Fig. S4), which further confirms that WS₂ is on the top of MoS₂ in the bilayer region.

Next, we used STM/STS to characterize the samples at atomic resolution. In our experiments, electrical contacts were thermally deposited through a shadow mask (Fig. 2a). A long focus optical microscope (Infinity K2) guided the STM tip onto individual heterobilayer islands, allowing the edges of the heterobilayer islands to be precisely located in large-scale STM survey (Fig. S5). Fig. 2b shows an STM image of a region containing both heterobilayer and MoS₂ monolayer. When zooming into the interfaces between the heterobilayer and MoS₂ monolayer, we observed, strikingly, a closed or continuous edge configuration (Fig. 2c). The atomically resolved STM image clearly exhibited that the top layer on the heterobilayer is seamlessly connected to the adjoining MoS₂ monolayer, implying a closed edge between the two regions (as illustrated in Fig. 2d). The continuity of the interfaces was observed on each edge of heterobilayer islands (Fig. S6b). The topography of these continuous interfaces between the monolayer and heterobilayer differs dramatically from the open edges of TMDs reported in the previously studies²⁶⁻²⁸, suggesting that the two layers were connected by covalent bonds at the edges of the top layer during the high temperature growth. The formation of new chemical bonds at the edges of 2D TMDs has been reported previously and was utilized to synthesize in-plane 2D heterostructures through a two-step CVD growth²⁹⁻³². The majority of the interfaces laid along the zigzag orientation, indicating that the zigzag edges were energetically more favorable

to form during the growth. This corroborates the previous theoretical calculations that the zigzag edge has a lower energy than the armchair edge³³. The interfaces were ~ 4 nm wide, and meandering slightly. The width and meandering could result from the underlying SiO₂ substrate being rough and/or the edges of the bottom layer being not atomically sharp. In addition to the interfaces between the heterobilayer and the monolayer, we also observed narrow trenches demarcating regions of bilayers (Figs. 2e, 2f and S6d). The trenches mostly laid along the zigzag orientation and were occasionally observed along the armchair orientation (Fig. S6d). These trenches were likely formed along parallel edges of neighboring bilayer islands, reflecting the gap between the bottom layers of the bilayer islands, whereas the top layers of the bilayer islands were continuously connected to each other.

The atomically resolved STM images (Fig. 2c and Fig. S6a) show that the lattice constant of the MoS₂ monolayer is 3.19 ± 0.05 Å and the lattice constant of the top layer (WS₂) of the heterobilayer is 3.20 ± 0.02 Å, respectively. The measured lattice constants are consistent with the previous theoretical calculations and experiment results³⁴⁻³⁸. The fast Fourier transform (FFT) images (the insets in Fig. 2c) reveal that the same crystalline orientation of the monolayer MoS₂ is the same as that of the top layer of the heterobilayer, corroborating the continuity of the monolayer and the top layer of the heterobilayer (Fig. 2d). Synthesized heterostructures have wide range of applications in electronics, optoelectronics, photovoltaics and catalysis. Clarifying the interface between the MoS₂ monolayer and the WS₂/MoS₂ heterobilayers is crucial for understanding the electronic and optical properties of such devices based on these heterostructures.

The height difference between the heterobilayer and the monolayer can be determined from the height histogram of an area straddling across the interface (the larger rectangle in Fig. 2b). The height histogram was fit well to a two-peak Gaussian function, reflecting a clear Gaussian distribution of heights for both the monolayer and heterobilayer (Fig. 3a). The only deviation from the fitting occurs around the middle of the two peaks, which is attributed to the continuous transition between the MoS₂ monolayer and the heterobilayer. For comparison, the height histogram of the areas away from the interfaces (areas marked in Fig. S6c) was fit perfectly to a two-peak Gaussian distribution with a zero probability in the middle of the two peaks (Fig. 3b). The height difference between the heterobilayer and the monolayer is determined by the distance

between the centers of the two peaks to be 0.837 ± 0.085 nm. This measured height is consistent with the height of a MoS₂ or WS₂ monolayer in the previous reports^{14, 30, 35}. From the width of the Gaussian peaks in the height histograms, we can also determine the roughness of MoS₂ monolayer and heterobilayer on SiO₂ surfaces. To reduce estimation errors due to the continuous interfaces between the monolayer and heterobilayer, we averaged the roughness evaluated from several areas on the monolayer and the heterobilayer away from the interfaces. The average RMS roughness is 0.329 ± 0.033 nm for the MoS₂ monolayer region and 0.230 ± 0.021 nm for the heterobilayer. Our result is consistent with the previously reported roughness of a MoS₂ monolayer on SiO₂³⁶. The monolayer roughness is also compatible with the roughness of a bare SiO₂ substrate previously measured by AFM³⁹⁻⁴⁰, indicating that the MoS₂ monolayer conformed well to the underneath SiO₂ surface. The slightly smoother topography of the heterobilayer is expected since the bending stiffness of the 2D material increases with thickness. A similar trend was observed in bilayer and monolayer graphene on SiO₂⁴¹. Moreover, the roughness of the heterobilayer is compatible with the previously reported roughness of a MoS₂ bilayer on SiO₂³⁶, implying that the stiffness of the heterobilayer is similar to that of MoS₂ bilayer.

After identifying the structures of the heterobilayer, the MoS₂ monolayer and their interface, now we turn to the electronic properties of these structures. We performed STS measurements at room temperature. At 77 K, the conductivity of the samples was too low to measure tunneling currents and the STM tip would crash into the samples. Therefore, all the STM/STS measurements were performed at room temperature. Fig. 4a shows the representative dI/dV curves obtained at the MoS₂ monolayer and the heterobilayer. In the averaged dI/dV curve, we linearly fitted the sloped parts that correspond to the conduction band. The conduction band edges are determined by extrapolating these linear lines to their crossings with the minimum conductance, while the valence band edges are determined by the peak positions at negative bias. The band gap is estimated by the separation of the valence band edge and conduction band edge (as shown in Fig. S7). For the MoS₂ monolayer, the measured band gap is 2.05 eV, with a conduction band edge at 0.75 eV and a valence band edge at -1.3 eV. These measured values are close to previously reported results on exfoliated monolayer MoS₂ on SiO₂^{18, 28}. For the heterobilayer, the band gap extracted from the averaged dI/dV curve is 1.35 eV, consistent with the previous results on MoS₂/WS₂ vertical heterobilayer on SiO₂ fabricated via the exfoliation method¹⁸. At the interface region, we performed the STS measurements at different locations

traversing the continuous interfaces (Figs. 4c and 4d). The transition from the heterobilayer type to the MoS₂ monolayer type occurs between dI/dV curves P8 and P9 in Figs. 4c and 4d. Although the electronic states previously found in open edges exhibited a distinct edge state²⁸, our results demonstrate the absence of edge states over the continuous transition regions between the MoS₂ monolayer and the heterobilayer.

To confirm our STS results, we carried out DFT calculations on a WS₂/MoS₂ heterobilayer, as well as individual MoS₂ and WS₂ monolayers (see Methods). In the simulation, the height of the heterobilayer differs from that of the monolayer by 6.15 Å, which is compatible to the measured height difference by STM. The theoretical height difference is from the bulk MoS₂. The calculated band structures (Fig. S8) show that the MoS₂ monolayer has a direct band gap of 1.72 eV at the K point, whereas the WS₂/MoS₂ heterobilayer has an indirect band gap of 1.26 eV with the valance band maximum (VBM) at the Γ point and the conduction band minimum (CBM) located between the K and Γ points. The decrease in band gap in the heterobilayer is in qualitatively good agreement with the experimental data, considering that DFT typically underestimates a band gap for semiconductors. As shown in Fig. 4b, when the Fermi level is set to zero, our calculated DOS plots for the MoS₂ monolayer and for the upper layer of the heterobilayer reveal a similar trend to the experimental dI/dV spectra below the Fermi level.

The DOS projected onto the top WS₂ layer in the heterobilayer (Fig. 4b) shows distinctive features near the Fermi level, compared to a free standing WS₂ monolayer (Fig. S9b). This change in the DOS may be attributed to the interlayer coupling between the MoS₂ and WS₂ monolayers, as explained below. To further analyze the nature of such coupling between the two different monolayers, as shown in Fig. S10, we calculated site- and orbital projected density of states (PDOS) for each atom in the MoS₂ and WS₂ monolayers and the heterobilayer, and clarified orbital characters of the VBM and CBM in each system. In the monolayers (Figs. S10i and S10j, where the WS₂ case is not shown since it is similar to the MoS₂ case), a contribution to the VBM arises mainly from the $d_{x^2-y^2}$ and d_{xy} orbitals of the transition metal atoms with a small contribution from the p_x and p_y orbitals of the sulfur atoms. The x , y , and z coordinates are illustrated in Fig. S10K. The CBM arises mainly from the d_{z^2} orbital of the metal atoms and the p_x and p_y orbitals of the sulfur atoms. Our results in the orbital analysis are consistent with the previous DFT study³⁷. Now regarding the heterobilayer (Figs. S10c-h), we find that the states

near the CBM predominantly originate mainly from the bottom MoS₂ layer, which corroborates with the type II band offset in the heterobilayer. The characteristics of the dominant orbitals near the CBM are not modified compared to the monolayer cases, which indicates that there is no effect of the interlayer coupling to the states near the CBM for the heterobilayer. This agrees with the experimental finding that the region near the CBM has not been affected upon building the heterobilayer (Fig. 4a). However, the orbital contributions near the VBM of the heterobilayer qualitatively change from the monolayer cases. In the heterobilayer, the DOS near the VBM mainly arises from the d_{z^2} orbitals of the molybdenum and tungsten atoms and the p_z orbitals of inner sulfur atoms, $S_{\text{Mo,in}}$ and $S_{\text{W,in}}$, as indicated in Fig. S10. Outer sulfur atoms ($S_{\text{Mo,out}}$ and $S_{\text{W,out}}$ in Fig. S10b) have negligible contributions to the VBM. The slightly higher contribution of the d_{z^2} orbitals of the tungsten atom than those of the molybdenum in the close proximity to the VBM, is consistent with the type II band offset. However, the d_{z^2} orbitals of both the molybdenum and tungsten atoms almost equally contribute to the shoulder region below the VBM (Figs. S10c and S10f). This shoulder region for the top WS₂ layer in the bilayer starts to appear about 0.25 eV below that in the MoS₂ monolayer (Fig. 4b), which agrees with the STS data (Fig. 4a). This change of the orbital characteristics in proximity to the VBM suggests substantial hybridization between the metal d_{z^2} orbitals and the inner sulfur p_z orbitals driven by a substantial interlayer interaction such as σ bonding.

Conclusion

In conclusion, we studied the morphology and electronic structures of as-grown MoS₂ monolayer and MoS₂/WS₂ heterobilayer on SiO₂ synthesized through the CVD method. The heterobilayer has a larger height than the monolayer with a height difference of 0.837 nm. The RMS roughness of the heterobilayer is 0.230 nm, compared with 0.329 nm for the monolayer. Most strikingly, we observed, for the first time, to the best of our knowledge, a closed interface between the MoS₂ monolayer and the heterobilayer with the atomic resolution. The discovery of such a nanostructure could deepen our understanding of the growth mechanism, interlayer interactions and electronic structures of 2D TMD heterostructures synthesized via CVD. Furthermore, our STS results and DFT calculations revealed band gaps of the heterobilayer and the MoS₂ monolayer agree with previously reported values for MoS₂ monolayer and MoS₂/WS₂

heterobilayer on SiO₂ fabricated through the mechanical exfoliation method. Our results could induce high impacts on optimizing and designing new 2D heterostructures.

Methods

Synthesis of MoS₂/WS₂ heterobilayers

Sulfur pieces (Alfa Aesar, 99.999 %, 1.5 g) and WO_{3-x}/MoO_{3-x} core/shell nanowires on ~2 mm×3 mm carbon fabric strips were used as S, W and Mo precursors, respectively²¹. The carbon fabric strip with WO_{3-x}/MoO_{3-x} core-shelled nanowires was directly placed on the top of a 300 nm SiO₂/Si substrate, and a ceramic boat with sulfur powder was placed upstream (Fig. S1). After purging the system with Ar for 15 min, the furnace was firstly heated up to 660 °C at a rate of 30 °C min⁻¹ with 150 sccm Ar and held for 25 min to vaporize the excessive MoO_{3-x}. The furnace was then heated up to 860 °C with a rate of 20 °C min⁻¹. When the furnace temperature reached 820°C, sulfur was heated by a heating belt with an individual temperature controller at ~200 °C. Then the furnace was cooled down naturally after maintaining 860 °C for another 30 min. The heating belt for sulfur was removed when the furnace was cooled down to 350 °C.

Oxidative etching of the heterobilayers

WS₂/MoS₂ heterobilayers were placed at the center of CVD furnace of a standard 1-inch quartz tube. After pumping down the system for 10 min, the furnace was heated up to 320 °C at a rate of 20 °C min⁻¹ and stayed for another 90 min.

Characterization of as-grown and etched heterobilayers

The optical images were taken with Olympus BX 51M microscope. AFM images were captured with Bruker Dimension Icon in tapping mode. Low-frequency Raman spectra were collected with WITEC RSA300+ Raman system under the 532 nm laser excitation with a power of 160 μW. Ordinary Raman spectra were carried out with Horiba-Jobin-Yvon Raman system under 532 nm laser excitation with a power of 2 mW. Raman and PL mapping images were performed by a step of 0.8 μm. The Si peak at 520 cm⁻¹ was used for calibration in the experiments.

STM and STS measurements

Au/Ti (80/10 nm) electrodes on the samples were fabricated by the masked thermal evaporation through a shadow mask. STM and STS characterizations were carried out in an ultra-high vacuum (UHV) STM system (a customized Omicron LT STM/Q-plus AFM system). The samples were annealed at 220 °C for 2 hours in the preparation chamber with a base pressure of $< 10^{-10}$ mbar. STM/STS measurements were then performed in the STM chamber that is connected to the preparation chamber. An optical microscope (Infinity K2) mounted to one of the optical windows of the STM chamber was used to precisely locate the STM tip to desired areas on the samples.

DFT calculations

We simulated MoS₂ and WS₂ monolayers and a WS₂/MoS₂ heterobilayers (i.e., a WS₂ monolayer on a MoS₂ monolayer) by DFT calculations using VASP⁴²⁻⁴³. We employed the Perdew-Burke-Ernzerhof (PBE) generalized-gradient approximation (GGA)⁴⁴ for the exchange-correlation functional and the projector-augmented wave (PAW) pseudopotentials⁴⁵. Spin-orbit coupling was included self-consistently in all calculations. Previous first-principles studies^{37, 46} reported that electronic structures of the TMD monolayers and homobilayers obtained from the PBE-GGA functional are similar to those from the GW method⁴⁷ or hybrid functionals such as Heyd-Scuseria-Ernzerhof (HSE06)⁴⁸, except for an underestimated band gap. Therefore, our choice of the functional was justified. For the MoS₂ and WS₂ monolayers, we used hexagonal unit cells with honeycomb structure (1H-MoS₂, 1H-WS₂) with experimental lattice constants and atomic coordinates⁴⁹⁻⁵². For the heterobilayers, we assumed AA' stacking equivalent to the 2H stacking of bulk MoS₂ or WS₂⁴⁶, because previous GW and DFT calculations on TMD homolayers revealed that the AA' stacking has the lowest energy; the AB stacking has an energy about 5 meV higher energy than the AA' stacking; the two stackings show very similar electronic structure⁴⁶. Regarding the WS₂/MoS₂ heterobilayer, we considered the experimental lattice constants of bulk MoS₂ (WS₂) for the MoS₂ (WS₂) monolayer, while adopting the vertical distance between monolayers, d , as the experimental value in bulk MoS₂. No further relaxation was carried out for the constructed heterobilayers. The choice of the heterobilayer geometry can

be justified, considering that the lattice constants of MoS₂ and WS₂ differ by less than 1%⁴⁹⁻⁵², and that the interlayer distance d agrees with the corresponding value in bulk TMD, even upon geometry relaxation⁴⁶. An energy cutoff was set to 300 eV and a k -point sampling of $27 \times 27 \times 1$ was applied. A vacuum layer thicker than 20 Å was included in a unit cell to avoid artificial interactions between neighboring bilayers. Van der Waals interactions were not included since our calculated DOS and PDOS did not change with their inclusion. We obtained the vacuum energy by calculating Hartree potential along the vertical axis, averaged over in-plane directions. The saturated value of Hartree potential in the vacuum region was identified to be the vacuum energy. To compare the band extrema of different systems and get the band alignment, we used the vacuum energy of each systems as a reference energy, and set it to zero.

We calculated the dipole moment of the heterobilayer and found a small value of $2.4 \times 10^{-3} \cdot \text{Å}$ and indeed, the change in the calculated vacuum energy was small upon including the dipole correction. Thus, we did not include the dipole correction in our calculations of the total and projected density of states, and the band structures. The interlayer distance was set to the experimental bulk value.

Supporting information Available:

Detailed description of the synthesis method, details about Raman and photoluminescence mapping of MoS₂ monolayer and WS₂/MoS₂ heterobilayer, additional STM results at various scales, and details about DFT calculations.

References

1. Mak, K. F.; Lee, C.; Hone, J.; Shan, J.; Heinz, T. F., Atomically Thin MoS₂: A New Direct-Gap Semiconductor. *Phys Rev Lett* **2010**, *105*, 136805.
2. Splendiani, A.; Sun, L.; Zhang, Y. B.; Li, T. S.; Kim, J.; Chim, C. Y.; Galli, G.; Wang, F., Emerging Photoluminescence in Monolayer MoS₂. *Nano Lett* **2010**, *10*, 1271-1275.
3. Ugeda, M. M.; Bradley, A. J.; Zhang, Y.; Onishi, S.; Chen, Y.; Ruan, W.; Ojeda-Aristizabal, C.; Ryu, H.; Edmonds, M. T.; Tsai, H. Z.; Riss, A.; Mo, S. K.; Lee, D. H.; Zettl, A.; Hussain, Z.; Shen, Z. X.; Crommie, M. F., Characterization of collective ground states in single-layer NbSe₂. *Nat Phys* **2016**, *12*, 92.
4. Tran, T. T.; Bray, K.; Ford, M. J.; Toth, M.; Aharonovich, I., Quantum emission from hexagonal boron nitride monolayers. *Nat Nanotechnol* **2016**, *11*, 37-41.
5. He, Y. M.; Clark, G.; Schaibley, J. R.; He, Y.; Chen, M. C.; Wei, Y. J.; Ding, X.; Zhang, Q.; Yao, W.; Xu, X. D.; Lu, C. Y.; Pan, J. W., Single quantum emitters in monolayer semiconductors. *Nat Nanotechnol* **2015**, *10*, 497-502.
6. Koperski, M.; Nogajewski, K.; Arora, A.; Cherkez, V.; Mallet, P.; Veuillen, J. Y.; Marcus, J.; Kossacki, P.; Potemski, M., Single photon emitters in exfoliated WSe₂ structures. *Nat Nanotechnol* **2015**, *10*, 503-506.
7. Radisavljevic, B.; Radenovic, A.; Brivio, J.; Giacometti, V.; Kis, A., Single-layer MoS₂ transistors. *Nat Nanotechnol* **2011**, *6*, 147-150.
8. Fang, H.; Chuang, S.; Chang, T. C.; Takei, K.; Takahashi, T.; Javey, A., High-Performance Single Layered WSe₂ p-FETs with Chemically Doped Contacts. *Nano Lett* **2012**, *12*, 3788-3792.
9. Lopez-Sanchez, O.; Lembke, D.; Kayci, M.; Radenovic, A.; Kis, A., Ultrasensitive photodetectors based on monolayer MoS₂. *Nat Nanotechnol* **2013**, *8*, 497-501.
10. Bie, Y. Q.; Grosso, G.; Heuck, M.; Furchi, M. M.; Cao, Y.; Zheng, J. B.; Bunandar, D.; Navarro-Moratalla, E.; Zhou, L.; Efetov, D. K.; Taniguchi, T.; Watanabe, K.; Kong, J.; Englund, D.; Jarillo-Herrero, P., A MoTe₂-based light-emitting diode and photodetector for silicon photonic integrated circuits. *Nat Nanotechnol* **2017**, *12*, 1124.
11. Rawal, T. B.; Le, D.; Rahman, T. S., Effect of Single-Layer MoS₂ on the Geometry, Electronic Structure, and Reactivity of Transition Metal Nanoparticles. *J Phys Chem C* **2017**, *121* (13), 7282-7293.

12. Novoselov, K. S.; Mishchenko, A.; Carvalho, A.; Neto, A. H. C., 2D materials and van der Waals heterostructures. *Science* **2016**, *353*, 461.
13. Yu, L. L.; Lee, Y. H.; Ling, X.; Santos, E. J. G.; Shin, Y. C.; Lin, Y. X.; Dubey, M.; Kaxiras, E.; Kong, J.; Wang, H.; Palacios, T., Graphene/MoS₂ Hybrid Technology for Large-Scale Two-Dimensional Electronics. *Nano Lett* **2014**, *14*, 3055-3063.
14. Hong, X. P.; Kim, J.; Shi, S. F.; Zhang, Y.; Jin, C. H.; Sun, Y. H.; Tongay, S.; Wu, J. Q.; Zhang, Y. F.; Wang, F., Ultrafast charge transfer in atomically thin MoS₂/WS₂ heterostructures. *Nat Nanotechnol* **2014**, *9*, 682-686.
15. Nourbakhsh, A.; Zubair, A.; Dresselhaus, M. S.; Palacios, T., Transport Properties of a MoS₂/WSe₂ Heterojunction Transistor and Its Potential for Application. *Nano Lett* **2016**, *16*, 1359-1366.
16. Ross, J. S.; Rivera, P.; Schaibley, J.; Lee-Wong, E.; Yu, H. Y.; Taniguchi, T.; Watanabe, K.; Yan, J. Q.; Mandrus, D.; Cobden, D.; Yao, W.; Xu, X. D., Interlayer Exciton Optoelectronics in a 2D Heterostructure p-n Junction. *Nano Lett* **2017**, *17*, 638-643.
17. Gong, C.; Zhang, H. J.; Wang, W. H.; Colombo, L.; Wallace, R. M.; Cho, K. J., Band alignment of two-dimensional transition metal dichalcogenides: Application in tunnel field effect transistors. *Appl Phys Lett* **2013**, *103* (5).
18. Hill, H. M.; Rigosi, A. F.; Rim, K. T.; Flynn, G. W.; Heinz, T. F., Band Alignment in MoS₂/WS₂ Transition Metal Dichalcogenide Heterostructures Probed by Scanning Tunneling Microscopy and Spectroscopy. *Nano Lett* **2016**, *16*, 4831-4837.
19. Zhang, T.; Jiang, B.; Xu, Z.; Mendes, R. G.; Xiao, Y.; Chen, L. F.; Fang, L. W.; Gemming, T.; Chen, S. L.; Rummeli, M. H.; Fu, L., Twinned growth behaviour of two-dimensional materials. *Nat Commun* **2016**, *7*, 13911.
20. Gong, Y. J.; Lin, J. H.; Wang, X. L.; Shi, G.; Lei, S. D.; Lin, Z.; Zou, X. L.; Ye, G. L.; Vajtai, R.; Yakobson, B. I.; Terrones, H.; Terrones, M.; Tay, B. K.; Lou, J.; Pantelides, S. T.; Liu, Z.; Zhou, W.; Ajayan, P. M., Vertical and in-plane heterostructures from WS₂/MoS₂ monolayers. *Nat Mater* **2014**, *13*, 1135-1142.
21. Zhang, Q.; Xiao, X.; Zhao, R. Q.; Lv, D. H.; Xu, G. C.; Lu, Z. X.; Sun, L. F.; Lin, S. Z.; Gao, X.; Zhou, J.; Jin, C. H.; Ding, F.; Jiao, L. Y., Two-Dimensional Layered Heterostructures Synthesized from Core-Shell Nanowires. *Angew Chem Int Edit* **2015**, *54*, 8957-8960.

22. Zhang, J.; Wang, J. H.; Chen, P.; Sun, Y.; Wu, S.; Jia, Z. Y.; Lu, X. B.; Yu, H.; Chen, W.; Zhu, J. Q.; Xie, G. B.; Yang, R.; Shi, D. X.; Xu, X. L.; Xiang, J. Y.; Liu, K. H.; Zhang, G. Y., Observation of Strong Interlayer Coupling in MoS₂/WS₂ Heterostructures. *Adv Mater* **2016**, *28*, 1950-1956.
23. Tongay, S.; Fan, W.; Kang, J.; Park, J.; Koldemir, U.; Suh, J.; Narang, D. S.; Liu, K.; Ji, J.; Li, J. B.; Sinclair, R.; Wu, J. Q., Tuning Interlayer Coupling in Large-Area Heterostructures with CVD-Grown MoS₂ and WS₂ Monolayers. *Nano Lett* **2014**, *14*, 3185-3190.
24. Wang, X. S.; Feng, H. B.; Wu, Y. M.; Jiao, L. Y., Controlled Synthesis of Highly Crystalline MoS₂ Flakes by Chemical Vapor Deposition. *J Am Chem Soc* **2013**, *135*, 5304-5307.
25. Cao, D.; Shen, T.; Liang, P.; Chen, X. S.; Shu, H. B., Role of Chemical Potential in Flake Shape and Edge Properties of Mono layer MoS₂. *J Phys Chem C* **2015**, *119*, 4294-4301.
26. Mills, A.; Yu, Y. F.; Chen, C. H.; Huang, B. V.; Cao, L. Y.; Tao, C. G., Ripples near edge terminals in MoS₂ few layers and pyramid nanostructures. *Appl Phys Lett* **2016**, *108*, 081601.
27. Chiu, M. H.; Zhang, C. D.; Shiu, H. W.; Chuu, C. P.; Chen, C. H.; Chang, C. Y. S.; Chen, C. H.; Chou, M. Y.; Shih, C. K.; Li, L. J., Determination of band alignment in the single-layer MoS₂/WSe₂ heterojunction. *Nat Commun* **2015**, *6*, 7666.
28. Zhang, C. D.; Chen, Y. X.; Huang, J. K.; Wu, X. X.; Li, L. J.; Yao, W.; Tersoff, J.; Shih, C. K., Visualizing band offsets and edge states in bilayer-monolayer transition metal dichalcogenides lateral heterojunction. *Nat Commun* **2016**, *7*, 10349.
29. Li, M. Y.; Shi, Y. M.; Cheng, C. C.; Lu, L. S.; Lin, Y. C.; Tang, H. L.; Tsai, M. L.; Chu, C. W.; Wei, K. H.; He, J. H.; Chang, W. H.; Suenaga, K.; Li, L. J., Epitaxial growth of a monolayer WSe₂-MoS₂ lateral p-n junction with an atomically sharp interface. *Science* **2015**, *349*, 524-528.
30. Chen, K.; Wan, X.; Wen, J. X.; Xie, W. G.; Kang, Z. W.; Zeng, X. L.; Chen, H. J.; Xu, J. B., Electronic Properties of MoS₂-WS₂ Heterostructures Synthesized with Two-Step Lateral Epitaxial Strategy. *Acs Nano* **2015**, *9*, 9868-9876.
31. Pant, A.; Mutlu, Z.; Wickramaratne, D.; Cai, H.; Lake, R. K.; Ozkan, C.; Tongay, S., Fundamentals of lateral and vertical heterojunctions of atomically thin materials. *Nanoscale* **2016**, *8*, 3870-3887.

32. Ling, X.; Lin, Y. X.; Ma, Q.; Wang, Z. Q.; Song, Y.; Yu, L. L.; Huang, S. X.; Fang, W. J.; Zhang, X.; Hsu, A. L.; Bie, Y. Q.; Lee, Y. H.; Zhu, Y. M.; Wu, L. J.; Li, J.; Jarillo-Herrero, P.; Dresselhaus, M.; Palacios, T.; Kong, J., Parallel Stitching of 2D Materials. *Adv Mater* **2016**, *28*, 2322-2329.
33. Xiao, S. L.; Yu, W. Z.; Gao, S. P., Edge preference and band gap characters of MoS₂ and WS₂ nanoribbons. *Surf Sci* **2016**, *653*, 107-112.
34. Kosmider, K.; Fernandez-Rossier, J., Electronic properties of the MoS₂-WS₂ heterojunction. *Phys Rev B* **2013**, *87*, 075451.
35. Huang, Y. L.; Chen, Y. F.; Zhang, W. J.; Quek, S. Y.; Chen, C. H.; Li, L. J.; Hsu, W. T.; Chang, W. H.; Zheng, Y. J.; Chen, W.; Wee, A. T. S., Bandgap tunability at single-layer molybdenum disulphide grain boundaries. *Nat Commun* **2015**, *6*, 6298.
36. Zhou, X. D.; Kang, K.; Xie, S.; Dadgar, A.; Monahan, N. R.; Zhu, X. Y.; Park, J.; Pasupathy, A. N., Atomic-Scale Spectroscopy of Gated Monolayer MoS₂. *Nano Lett* **2016**, *16*, 3148-3154.
37. Kang, J.; Tongay, S.; Zhou, J.; Li, J. B.; Wu, J. Q., Band offsets and heterostructures of two-dimensional semiconductors. *Appl Phys Lett* **2013**, *102*, 012111.
38. Zhu, Z. Y.; Cheng, Y. C.; Schwingenschlogl, U., Giant spin-orbit-induced spin splitting in two-dimensional transition-metal dichalcogenide semiconductors. *Phys Rev B* **2011**, *84*, 153402.
39. Ishigami, M.; Chen, J. H.; Cullen, W. G.; Fuhrer, M. S.; Williams, E. D., Atomic structure of graphene on SiO₂. *Nano Lett* **2007**, *7*, 1643-1648.
40. Quereda, J.; Castellanos-Gomez, A.; Agrait, N.; Rubio-Bollinger, G., Single-layer MoS₂ roughness and sliding friction quenching by interaction with atomically flat substrates. *Appl Phys Lett* **2014**, *105*, 053111.
41. Lauffer, P.; Emtsev, K. V.; Graupner, R.; Seyller, T.; Ley, L.; Reshanov, S. A.; Weber, H. B., Atomic and electronic structure of few-layer graphene on SiC(0001) studied with scanning tunneling microscopy and spectroscopy. *Phys Rev B* **2008**, *77*, 155426.
42. Kresse, G.; Furthmuller, J., Efficient iterative schemes for ab initio total-energy calculations using a plane-wave basis set. *Phys Rev B* **1996**, *54*, 11169-11186.
43. Kresse, G.; Furthmuller, J., Efficiency of ab-initio total energy calculations for metals and semiconductors using a plane-wave basis set. *Comp Mater Sci* **1996**, *6*, 15-50.

44. Perdew, J. P.; Burke, K.; Ernzerhof, M., Generalized gradient approximation made simple. *Phys Rev Lett* **1996**, *77*, 3865-3868.
45. Blochl, P. E., Projector Augmented-Wave Method. *Phys Rev B* **1994**, *50*, 17953-17979.
46. He, J. G.; Hummer, K.; Franchini, C., Stacking effects on the electronic and optical properties of bilayer transition metal dichalcogenides MoS₂, MoSe₂, WS₂, and WSe₂. *Phys Rev B* **2014**, *89*, 075409.
47. Aryasetiawan, F.; Stott, M. J., Effective Potentials in Density-Functional Theory. *Phys Rev B* **1988**, *38*, 2974-2987.
48. Heyd, J.; Scuseria, G. E.; Ernzerhof, M., Hybrid functionals based on a screened Coulomb potential. *J Chem Phys* **2003**, *118*, 8207-8215.
49. Bronsema, K. D.; Deboer, J. L.; Jellinek, F., On the Structure of Molybdenum Diselenide and Disulfide. *Z Anorg Allg Chem* **1986**, *541*, 15-17.
50. Schutte, W. J.; Deboer, J. L.; Jellinek, F., Crystal-Structures of Tungsten Disulfide and Diselenide. *J Solid State Chem* **1987**, *70*, 207-209.
51. Wyckoff, R. W. G., Crystal Structures. Interscience Publishers, New York, New York **1963**, *1*, 280-281.
52. Momma, K.; Izumi, F., VESTA 3 for three-dimensional visualization of crystal, volumetric and morphology data. *J Appl Crystallogr* **2011**, *44*, 1272-1276.

Acknowledgements

F.Z., H.Z. and C.T. acknowledge the financial support provided for this work by the U.S. Army Research Office under the grant W911NF-15-1-0414. L.J. acknowledges National Natural Science Foundation of China (No.51372134, No.21573125) and Tsinghua University Initiative Scientific Research Program. L.X. acknowledges NSFC (Nos. 21373066 and 21673058), Key Research Program of Frontier Sciences of CAS (QYZDB-SSW-SYS031), Strategic Priority Research Program of CAS (XDA09040300), Beijing Nova Program (Z151100000315081) and Beijing Talents Fund (2015000021223ZK17). Y. C. was supported by the ICTAS fellowship at Virginia Tech, and the computational support was provided by San Diego Supercomputer Center (SDSC) under DMR060009N and Virginia Tech Advanced Research Center.

Figures

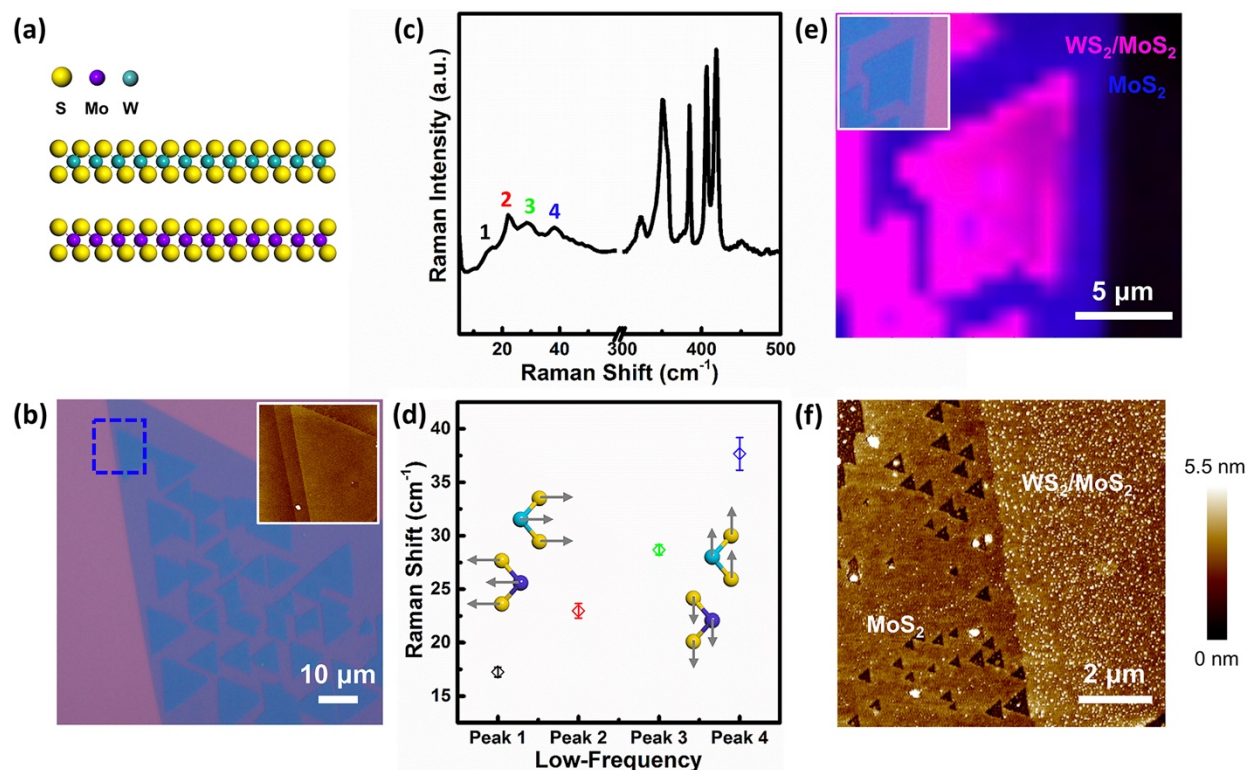


Fig. 1. (a) Schematic of WS_2/MoS_2 vertical heterostructures. (b) Optical image of WS_2/MoS_2 vertical heterostructures. Inset, AFM image of WS_2/MoS_2 vertical heterostructures in the blue rectangle. (c) Raman spectra of WS_2/MoS_2 vertical heterostructures. (d) Distributions of low-frequency Raman modes. Peaks 1 and 2 correspond to the shear modes, and Peaks 3 and 4 correspond to the layer breathing modes. (e) Raman mapping of MoS_2 monolayer and MoS_2/WS_2 vertical heterostructures in the inset. (f) AFM height image of MoS_2 monolayer and WS_2/MoS_2 vertical heterostructures by oxidative etching in 320°C .

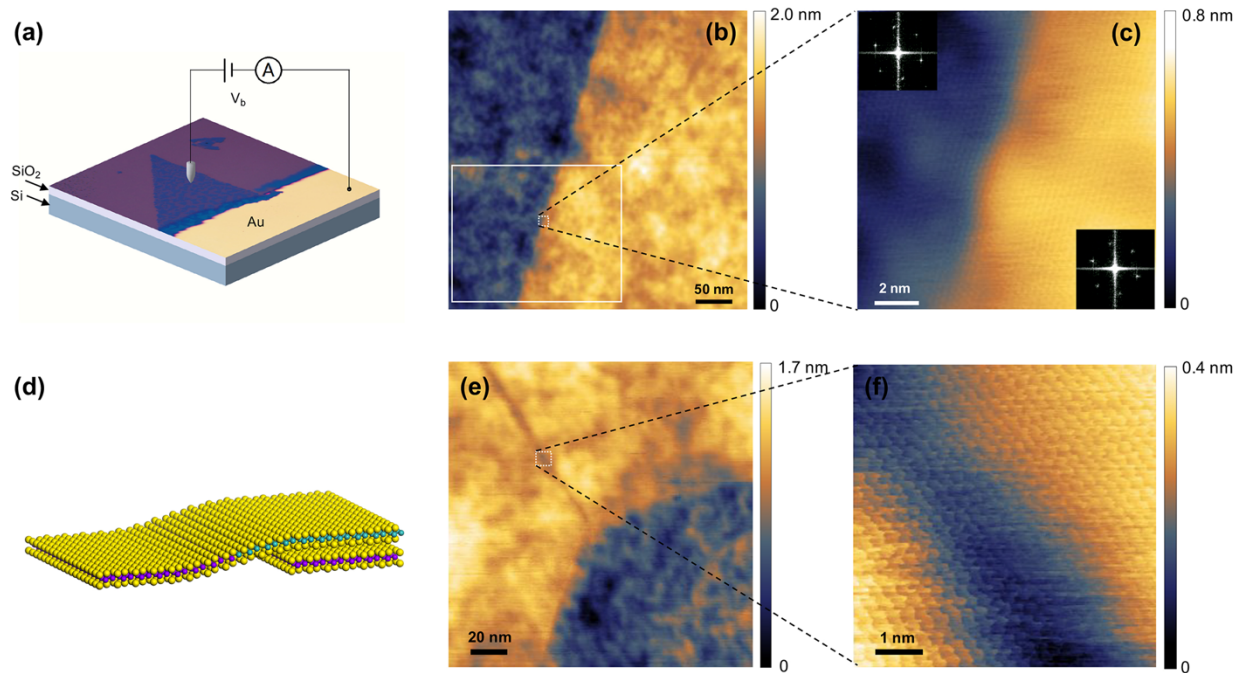


Fig. 2. (a) Schematic illustration of the experiment setup for STM/STS coupled with optical imaging. (b) Large-scale STM image of the MoS₂ monolayer and the heterobilayer ($V_s = 1$ V, $I = 0.1$ nA). (c) Atomically resolved STM image of the interface between the monolayer and the heterobilayer, marked by the dashed white rectangle in (b) ($V_s = 1$ V, $I = 0.15$ nA). Insets, FFT of the monolayer region and heterobilayer region, respectively. (d) Schematic drawing of the interface between the heterobilayer and the MoS₂ monolayer. (e) Large-scale STM image of a trench structure demarcating the heterobilayer ($V_s = -0.55$ V, $I = 0.3$ nA). (f) Atomically resolved STM image of the trench structure, marked by the dashed white rectangle in (e) ($V_s = 1.1$ V, $I = 0.2$ nA).

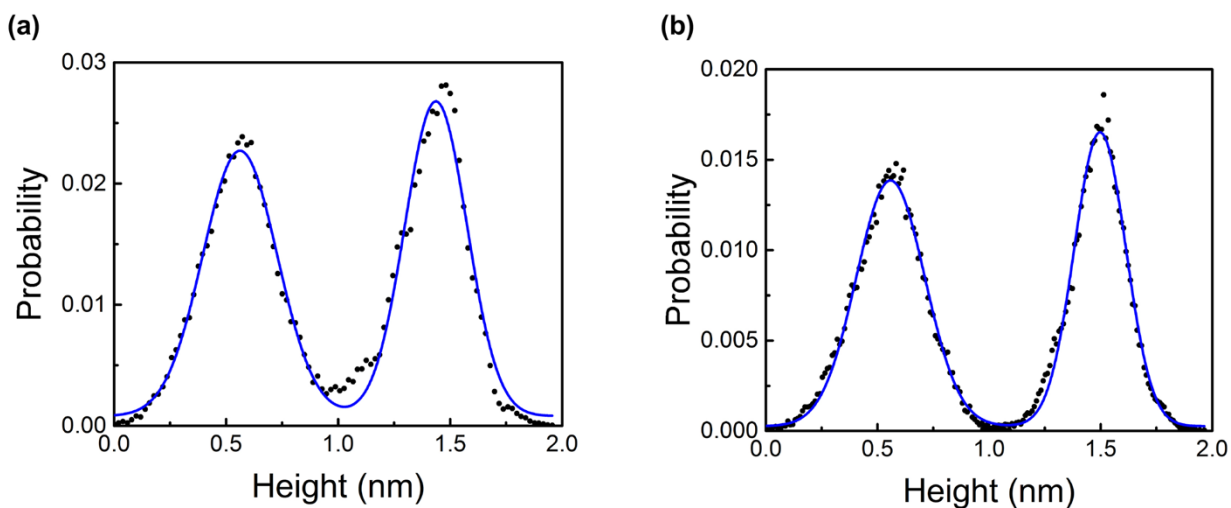


Fig. 3. (a) Height histogram of the area marked by the solid white rectangle in Fig. 2b, which includes the interface between the MoS₂ monolayer and the heterobilayer. Blue line: two-peak Gaussian fitting of the height histogram. (b) Height histogram of areas containing only the MoS₂ monolayer and the heterobilayer, without an interface between the MoS₂ monolayer and the heterobilayer. Blue line: two-peak Gaussian fitting of the height histogram.

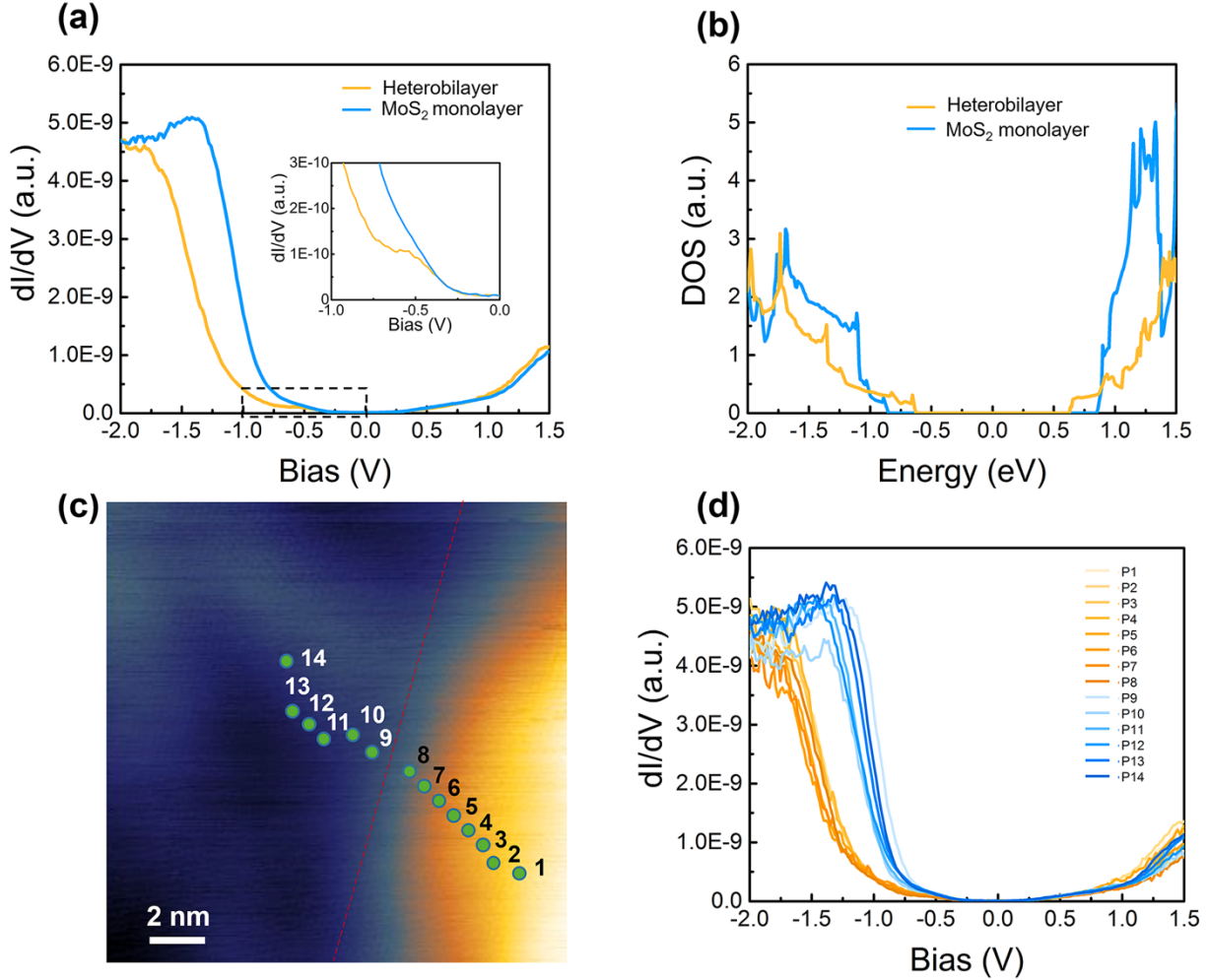


Fig. 4. (a) Experimental dI/dV spectra for the MoS₂ monolayer (blue) and the heterobilayer (yellow). Inset shows expanded view of dI/dV spectra between -1.0 and 0.0 V. (b) DFT-calculated density of states (DOS) of the MoS₂ monolayer (blue) and DOS projected onto the top WS₂ layer in the WS₂/MoS₂ heterobilayer (yellow). Here the Fermi level was set to zero. (c) STM image of the interface between the MoS₂ monolayer and the heterobilayer ($V_s = 1V$, $I = 0.15$ nA). The interface is marked by the dashed red line. (d) dI/dV spectra acquired at the points marked in (c).